Design and Experimental Performance Assessment of an Outer Rotor PM-Assisted SynRM for the Electric Bike Propulsion

Reza Nasiri-Zarandi, *Member, IEEE*, Ahmadreza Karami-Shahnani, *Member, IEEE*, Mohammad Sedigh Toulabi, *Senior Member, IEEE*, and Alberto Tessarolo, *Senior Member, IEEE*

***Abstract*— Brushless dc motor (BLDCM) is a conventional machine type used in the electric bike (e-bike) industry due to its simple controllability and drive system. However, the fluctuating price and scarcity of NdFeB magnets used in BLDCMs, lower power density compared to ac machines, and high torque ripple have pushed researchers in industry and academia to investigate technology alternatives to BLDCMs in e-bike applications. Permanent magnet-assisted synchronous reluctance motor (PMaSynRM) is an attractive option to this end because of its adjustable reluctance torque component and the recent advancements in finite-element (FE)-based design algorithms and implementation. Not yet covered in the existing literature and industry reports for e-bike applications, an in-hub outer rotor PMaSynRM is designed in this article to improve the power density and reduce the torque ripple characteristics for replacing a 500-W commercial BLDCM. The designed PMaSynRM is fabricated and tested to validate the power density and torque ripple improvements compared to an existing Golden Motor MP2 BLDCM counterpart.**

***Index Terms*— Brushless dc motor (BLDCM), electric bike (e-bike), in-hub outer rotor, performance comparison, permanent magnet-assisted synchronous reluctance motor (PMaSynRM).**

I. Introduction

ELECTRIC bikes (e-bikes) have been popular even since the beginning of the 20th century, but their worldwide industrialization failed due to the lack of advanced technologies in electric motor design, battery limitations, and power electronics devices and control. However, due to the current high price and shortage of fossil fuels and environmental concerns, electric vehicles (EVs), including e-bikes, have become a major point of interest again for both industry and academia [1], [2].

This work was supported by Niroo Research Institute (NRI), Tehran, Iran. *(Corresponding author: Reza Nasiri-Zarandi.)*

Reza Nasiri-Zarandi is with the Electrical Machine Research Department, Niroo Research Institute (NRI), Tehran 1468613113, Iran (e-mail: rnasirizarandi@nri.ac.ir).

Ahmadreza Karami-Shahnani is with the Department of Electrical Engineering, K. N. Toosi University of Technology, Tehran 1631714191, Iran (e-mail: ar.karami@email.kntu.ac.ir).

Mohammad Sedigh Toulabi is with the Department of Electrical and Computer Engineering, University of Windsor, Windsor, ON N9B 3B4, Canada (e-mail: toulabi@uwindsor.ca).

Alberto Tessarolo is with the Engineering and Architecture Department, University of Trieste, 34127 Trieste, Italy (e-mail: atessarolo@units.it).

Digital Object Identifier 10.1109/TTE.2022.3202819

Three types of e-bikes are currently available in the market. In type 1, called pedal-assist or pedelec e-bikes, the bicycle rider is assisted by a low-power electric motor [3]. In type 2, called throttle, the bike is ridden without any pedaling power and is driven by an electric motor. The speed of e-bikes of types 1 and 2 is limited to 32 km/h and can be used in places where traditional speed bicycle riding is permitted [4]. Type three of e-bikes is similar to type 1, but its speed may be increased up to 45 km/h. Due to the higher speed allowed in type three e-bikes, they are banned from certain bike trails and paths. The output power, weight, and maximum speed ratings for sample existing commercial e-bikes are collected and presented in Fig. 1(a). As mentioned before, the price of an e-bike does not depend on the electric motor. In addition to the electric motor, the battery and control unit are the other factors affecting the price of e-bikes. To have a better view about the cost of selected e-bikes, the per-unit costs based on the most expensive studied e-bikes are presented in Fig. 1(b) based on their power and battery capacity.

As it can be seen, there are various combinations of power, weight, and maximum speed for different e-bikes and each of them may be used depending on the applications and regulations. In terms of the electric motor installation arrangement, e-bikes are classified into three types: back-wheel hub motor, mid-drive motor, and front-wheel hub motor [3]. In the hub-drive e-bikes, the wheel/wheels bear the extra motor weight reducing the flexibility on rough terrains. In mid-drive e-bikes, the motor weight is shared between two wheels, and it provides more flexibility and space for utilizing the gearbox. Based on Fig. 1, most commercial e-bikes belonging to type 1 or 2 possess a mid-drive configuration with a gearbox and their output powers are limited to only 250 W [4], [5], [6]. Using gearbox increases the maintenance and transmission losses and reduces the reliability of the e-bikes. Besides, the complexity of the mid-drive structure makes them more expensive than the other two types. These limitations justify using high power and torque density motors to cope with space constraints in direct drive arrangements [7], [8].

Permanent magnet (PM) machines are frequently used in EV applications due to their remarkable strengths such as the possibility to operate over a wide speed range [2], [9]. Brushless dc motors (BLDCMs), as a subcategory of PM machines, have been commercialized as a conventional option for e-bike

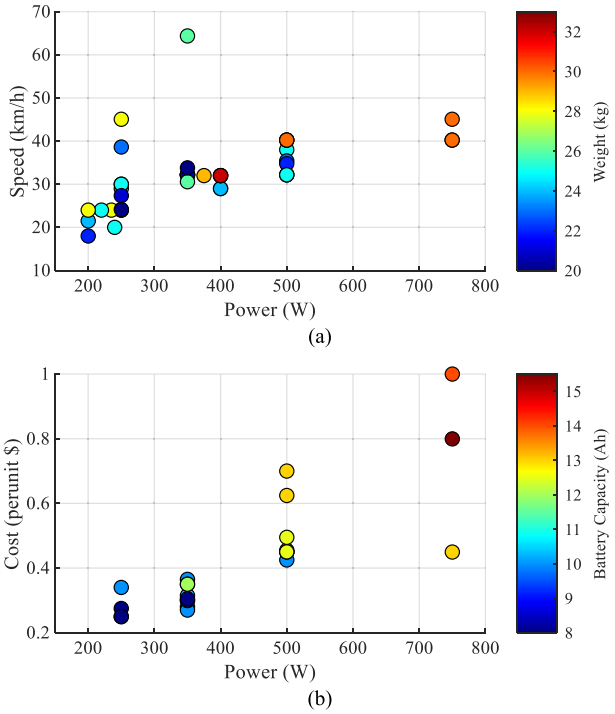

Fig. 1. (a) Maximum speeds and weights distribution. (b) Per-unit cost and battery capacity of sample existing commercial e-bikes versus electric motor powers.

propulsion complying with a variety of performance standards [7]. The main reason for the popularity of BLDCMs is the simplicity of their control and drive systems [10]. However, to satisfy the high power and torque density requirements, the expensive rare-earth PMs (e.g., NdFeB magnets) are normally used in the motor structure. The harmful environmental impact of rare-earth PMs as well as their limited availability increase the final product cost [11]. In addition, BLDCMs may have a lower power capability and higher torque ripple compared to conventional ac machines due to commutations and trapezoidal shape of their back EMF waveform [12].

In order to select and design a BLDCM, as well as any other types of electric motors for e-bike applications, some constraints with major impacts on e-bike performance should be taken into consideration as highlighted next.

1) *Cost and Materials Availability:* The electric motor price has a significant impact on the e-bike overall cost. Due to the competition among manufacturers, using a low-cost motor built from widely available materials on the market is a strongly preferred option, if viable [7].
2) *Volume and Weight:* The volume and weight of an e-bike are usually limited by national regulations. These parameters are also affected by the available space, structure stability, and motor output power, which are all critical constraints for e-bike users. It is a matter of fact that most of the e-bike weight comes from the installed electric motor [4], [5], [6], [13].
3) *Torque Ripple:* The high torque ripple is a disturbing factor that a rider may feel due to the low inertia and weight of e-bikes. Hence, the motor torque ripple should be reduced as much as possible.
4) *Efficiency:* In the EV industry, the overall system efficiency is one of the important factors in battery lifetime and performance [7]. The electric motor efficiency, in particular, plays a significant role in terms of battery usage.

Various studies and research have investigated the design and implementation of PM-based machines for EV propulsion, which are not well suited for an e-bike, though, considering the constraints listed above [8], [14]. BLDCMs with a high number of rotor poles are the most common motor type for commercial lightweight EVs due to their advantages such as encouraging torque density and simple control and drive methods [7], [15]. However, they mainly suffer from a noticeable amount of expensive PMs in their structure, low thermal, and overload capability due to PMs, demagnetization risks, difficult fabrication, and vibration issues [9], [15]. To overcome these shortcomings, reluctance motors (RMs) have been widely utilized in various applications [9]. The rotor of an RM has no PMs (or very few in some types), making RMs cheaper and more environmentally sustainable compared to PM-based machines. The RMs are classified into three main categories: switched reluctance motors (SRMs), synchronous reluctance motors (SynRMs), and permanent magnet-assisted synchronous reluctance motors (PMaSynRMs). Due to the simple fabrication procedure and high resilience to faults, SRMs are attractive alternatives to other machine types for EVs [16]. A direct-drive SRM has been analytically designed for an e-bike in [7] and [17]. Nonetheless, SRMs suffer from high torque ripple and noise making them incompatible with lightweight EV applications such as e-bikes. In SynRMs, flux barriers provide the reluctance torque component by increasing the difference between the d-axis and q-axis inductance values. Although SynRMs, such as SRMs, benefit from robustness against mechanical stress and faults, they have a low power factor, torque density, and overload capability due to magnetic saturation. These drawbacks limit their application in EVs [18].

A possible method to improve the relatively low torque density and power factor (PF) in a SynRM is to add PMs to the rotor structure of the machine making it a PMaSynRM. This article presents a 500-W, 210-r/min, direct-drive outer rotor PMaSynRM configuration for an in-hub, type 2 e-bike to benefit from its advantages such as simple and rigid construction, hazard-less operations, and low cost. Over one half of the total torque of the designed PMaSynRM is provided by the reluctance component and the total volume of the machine as well as the amount of utilized PMs are minimized through the design procedure to improve the torque density, torque ripple, and costs. After a detailed description of the design methodology employed, simulations and laboratory tests on a prototype are presented to compare the performance characteristics and physical dimensions of the designed PMaSynRM with those of a BLDCM utilized in a commercial existing e-bike. The results validate the proposed solution as an innovative, feasible, and interesting option for e-bike propulsion and provide the guidelines for adapting the same technology to other possible power ratings and specifications.

TABLE I

AVERAGE TORQUES, TORQUE RIPPLES, AND POWER FACTORS FOR DIFFERENT (PMA)SYNRMS

PM Type	Two Flux Barriers [T_{avg}(N.m), T_{ripple}(%), PF]		Three Flux Barriers [T_{avg}(N.m), T_{ripple}(%), PF]	
	Non-Skewed	Skewed	Non-Skewed	Skewed
None (SynRM)	[12.5, 87, 0.63]	[11.7, 18, 0.64]	[14.0, 31, 0.67]	[13.9, 5.2, 0.66]
Rare-earth	[17.2, 104, 0.83]	[16.8, 11, 0.89]	[22.3, 35, 0.87]	[22.0, 3.4, 0.88]
Non-Rare Earth	[17.1, 76, 0.75]	[16.1, 11, 0.76]	[19.6, 25, 0.80]	[18.9, 5.2, 0.79]

II. MOTOR SELECTION FROM THE FEASIBLE CHOICES

In this section, various steps are taken to introduce a baseline PMaSynRM as a suitable motor candidate for subsequent design refinements and modifications. The low PF and torque density of SynRMs lead to a higher power demand for motor supply and control, so from a system-level perspective, an e-bike based on a SynRM can be more expensive than one using a PM synchronous motor (PMSM). PMaSynRMs benefit from both reluctance and magnetic torque components simultaneously. This topology needs less PMs than in PMSMs because a significant portion of the torque results from the reluctance component. By adjusting the saliency ratio, the individual contribution of the reluctance and magnetic torques can be tuned in the total torque profile [18]. Based on the specific goals and constraints mentioned in Section I, a proper PMaSynRM design can be a solution to decrease the PM cost of BLDCMs and PMSMs and overcome the low torque density (high volume and weight) and high torque ripple of SRMs and SynRMs. Paying attention to the magnetic and physical limitations and constraints typical of e-bike applications, all the promising initial designs are identified considering the torque performance in various possible PMaSynRM configurations.

For the purpose of a qualitative preliminary assessment, FE-based comparative results are presented in Table I for a sample 500-W, 210-r/min, outer rotor (PMa)SynRM in the maximum torque per ampere (MTPA) region assuming skewed/nonskewed stator, two or three flux barrier rotors with and without magnets. In Table I, T_{avg} and T_{ripple} are the average electromagnetic torque and torque ripple, respectively. The comparison shows that the torque ripple and average torque in skewed PMaSynRM with rare-earth PMs can be even 35% lower and 58% higher, respectively, than in SynRM. Also, it shows that using PM can improve the PF by 19%–35%.

The preliminary study suggests that the models with nonskewed stators have high torque ripple values that make them inapplicable to e-bike propulsion. Furthermore, one can infer that by increasing the number of flux barriers, both the average torque and torque ripple increase. Fig. 2 shows the steady-state torque profiles for SynRMs with two and three flux barrier rotors. The average torque and torque ripple values are 12.5 N · m and 87% for two flux barrier rotors and

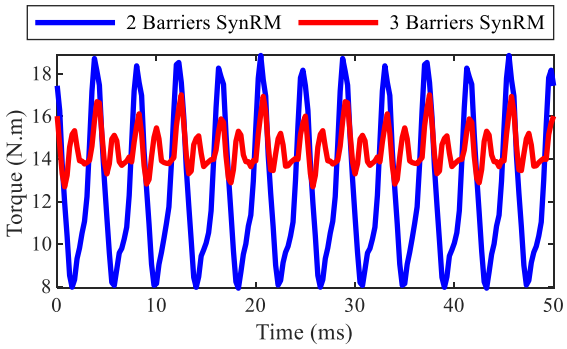

Fig. 2. Steady-state torque profiles of SynRMs with a different number of flux barriers and the same nonskewed stator.

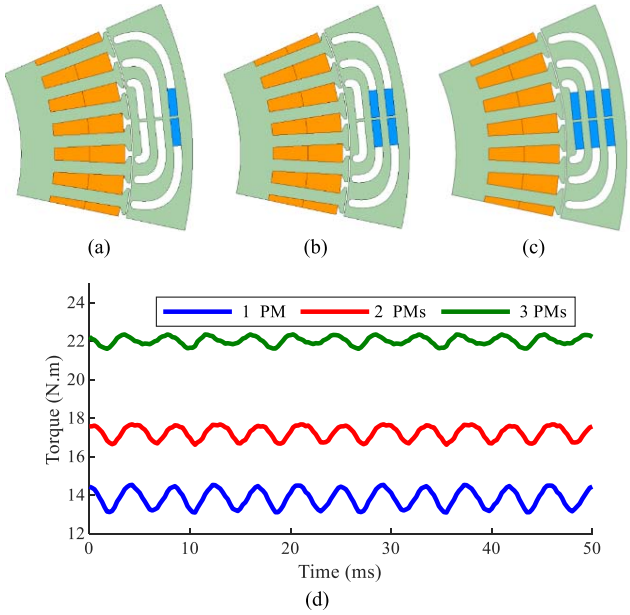

Fig. 3. One pole of the investigated PMaSynRMs with various numbers of PMs and corresponding torque profiles. (a) One PM. (b) Two PMs. (c) Three PMs. (d) Steady-state torques.

14 N · m and 31% for three flux barrier rotor. Furthermore, as the number of flux barriers grows the saliency ratio rises too, leading to an improved motor performance. It is worth noting that the number of flux barriers is limited to three due to mechanical constraints.

To fulfill the e-bike requirements of 500 W at 210 r/min, a PMaSynRM with N35 rare-earth PMs and three flux barriers per pole is selected as the baseline structure. To search for the best number of flux barriers including the PMs, an analysis on the output torque is conducted by the FE analysis (FEA) and the results are reported in Fig. 3. One pole of the proposed PMaSynRM with different PM configurations is shown in Fig. 3(a)–(c), and the instantaneous torque for each of the options is presented in Fig. 3(d). As the results have shown, the three-flux-barrier design with slots fully occupied by PMs along the q-axis can meet the requirements of the average torque and torque ripple via the available commercial N35 rare-earth PMs. Thus, as the baseline structure, an outer rotor PMaSynRM with a skewed stator and a rotor with three flux barriers filled by PMs is selected as an appropriate choice for the following design refinements and modifications.

Fig. 4. Commercial BLDCM mounted on an e-bike in the lab with relevant dimensional constraints.

TABLE II
MOTOR DESIRED RATED SPECIFICATIONS AND DIMENSIONS

Parameter	Symbol	Unit	Value
Rated Power	P	W	500
Battery Voltage	V	V	48
Rated Speed	N	rpm	200
Efficiency	η	%	65-70
Torque Ripple	-	%	≤10
Stack Length	L_{stk}	mm	≤ 30
Rotor Outer Diameter	D_o	mm	≤270

III. DESIGN PROCESS AND FINAL ROTOR STRUCTURE FOR THE PMASYNRM

In this section and based on the preliminary design choices discussed in Section II, the dimensions of the PMaSynRM are sought to minimize the total active volume of the machine and PMs as well as the torque ripple and total cost while increasing the torque density.

Some of the design parameters are limited by the type of e-bike that is selected for the final application. Fig. 4 shows the e-bike that mounts the Golden Motor MP2 BLDCM as the propulsion motor, for which significant ratings and design data are shown in Table II. The maximum available space for the motor installation, including the outer diameter (D_{max}) and stack length (L_{stk}), is shown in Fig. 4. Since the PMaSynRM is an alternative to the existing BLDCM, the motor outer diameter and axial length are limited to 270 and 70 mm, respectively. The other desired specifications for the PMaSynRM are listed in Table II.

A PMaSynRM is designed by a two-step process. The motor general dimensions, stator structure, and distributed winding parameters are designed based on the conventional ac machine design procedure [18] in the first step. Due to higher torque ripple, higher iron loss because of the flux harmonics, machine's saliency ratio reduction due to a higher leakage flux, and PM demagnetization risks, the concentrated winding configurations are not utilized in the designed (PMa)SynRMs

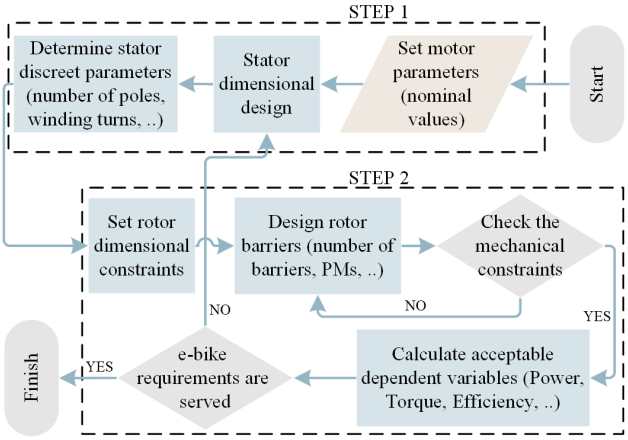

Fig. 5. Implemented FE-based PMaSynRM design process and its steps.

in this article. However, the main issue is the design of the rotor flux barriers, which will be conducted in the second step. The saliency ratio (ξ) is defined as the ratio between d- and q-axis inductances (Ld and Lq). Having a large value for ξ leads to high reluctance torque and power factor [19]. The overall torque is calculated as in (1) for PMaSynRMs [18]

$$T_{em} = \frac{3}{2} p \times i_d\big((L_d - L_q) i_q + \lambda_{PM}\big) \tag{1}$$

where T_{em} is the average developed torque, p is the number of motor pole pairs, i_d and i_q are d- and q-axis currents, respectively, and λ_{PM} is the PM flux linkage.

Although some analytical approaches are available to model RMs [19], using FEA is one of the most accurate methods, especially when the rotor experiences local saturations. The implemented two-step PMaSynRM design process described in Fig. 5 employs FEA to calculate power, torque, and efficiency.

In the first step, the stator design process is conducted. In this stage, the rated parameters based on BLDCM (Table II) are fixed. Then, the discrete variables for design parameters, i.e., the number of poles and stator slots, are determined by considering the rate of the required torque and the specified mechanical constraint (weight and volume). Next, the winding configuration, including the coil span, fill factor, and allowed temperature, are determined.

In the second step, the rotor design process is performed. The detail of rotor design parameters is presented in the next paragraphs. At the end, the dependent variables, such as efficiency, power factor, and torque, are calculated using the FEA according to the constraints and the permitted range of the independent variables. In this way, some valid designs will be generated where all the designs are within the desired range.

All valid designs are selected based on the physical and mechanical requirements for the e-bike. Three of the most suitable designs fitting the e-bike application are presented in Table III where the finally selected design is provided in the third row of Table III as it possesses 9% and 5% higher torque densities compared to the other two given in rows 1 and 2, respectively. In Table III, the Eff., P.F., T, and ρT represent

TABLE III

CHARACTERISTICS OF THREE FEASIBLE VALID PMASYNRM DESIGNS

Independent Variables				Dependent Variables			
P [W]	N [rpm]	D_o [mm]	L_{stk} [mm]	*Eff.* [%]	*P.F.*	T [N.m]	ρT [N/m^3]
500	200	270	37.5	66.07	0.72	26.26	12.2
550	220	270	33	67.20	0.72	23.87	12.6
500	210	270	30	67.86	0.71	22.80	13.3

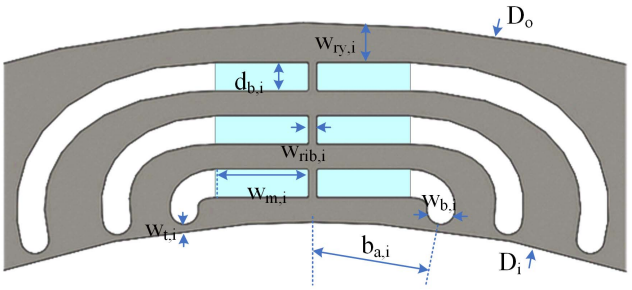

Fig. 6. Different design variables for the rotor of the finally designed PMaSynRM with PMs highlighted in light blue.

the calculated FEA-based efficiency, power factor, torque, and torque density, respectively.

Due to the special rotor structure in SynRMs, the applicable rotor design process needs special considerations. The proper shape of the flux barriers has noticeable impacts on the magnetic torque characteristics [18], [19], [20], [21], [22], [23]. The high number of rotor dimensional variables makes the design procedure complicated. These variables are shown in Fig. 6 where the i-subscript is the variable counter. A detailed geometry analysis of the rotor structure for PMaSynRM is presented in [23], which is utilized in the design procedure. Since the rotor has more than 20 design variables, it is recommended to define the barriers dimensional variables, called free variables, based on the constrained variables, e.g., D_o and D_i in the final design selection process. In this way, the proper value for the free variables in the final design selection will be possible without reducing the number of variables. According to (1), the lower Lq or the higher Ld, the larger the average torque will be. To this end, the permeance along the q-axis should be as low as possible. The minimum value of Lq is limited by the rotor saturation that is related to the pole flux as highlighted in (2). The w_{ry} parameters play an important role on the rotor pole flux and, consequently, the value of Lq that is calculated as

$$w_{ry,i} = \frac{(D_o - D_i)(1 - k_{\text{air}})B_{\text{avg},i}}{2\sum_{i=1}^{N_b+1} B_{\text{avg},i}}. \tag{2}$$

The parameters in (2) are graphically specified in Fig. 6. Also, $B_{\text{avg},i}$ is the average flux density in the ith iron part, which can be calculated analytically or by the FEA method, and N_b is the number of barriers. In the rotor design process for PMaSynRM, the coefficient k_{air} is defined as in (3). Once k_{air} is defined, the total widths of the barriers and iron parts

TABLE IV

FINAL PARAMETERS FOR THE ROTOR STRUCTURE OF THE DESIGNED PMASYNRM

Parameter	Unit	Value
$\{w_{ry1}, w_{ry2}, w_{ry3}, w_{ry4}\}$	mm	{3.43, 2.74, 2.74, 2.74}
$\{d_{b1}, d_{b2}, d_{b3}\}$	mm	{4.09, 4.09, 3.47}
$\{w_{m1}, w_{m2}, w_{m3}\}$	mm	{10, 13.09, 12.9}
$\{w_{t1}, w_{t2}, w_{t3}\}$	mm	{1.5, 1.5, 1.5}
$\{b_{a1}, b_{a2}, b_{a3}\}$	rad	{0.12, 0.19, 0.27}
$\{w_{b1}, w_{b2}, w_{b3}\}$	mm	{2.08, 3.07, 3.47}

are determined. The width of each iron part is then computed according to (2) and the flux density distribution of the d-axis flux. Raising k_{air} increases the flux density in the rotor and decreases d-axis flux linkage, which causes a reduction in torque and power [18]

$$k_{\text{air}} = \frac{\sum_{i=1}^{N_b} d_{bi}}{\sum_{i=1}^{N_b} d_{bi} + \sum_{i=1}^{N_b+1} w_{ryi}} \leq 1. \tag{3}$$

Various goals during the design process can be considered to have an applicable rotor structure, such as maximizing the torque, maximizing the saliency ratio, or maximizing the difference between Ld and Lq. For the designed PMaSynRM of this article, maximizing the difference between Ld and Lq, total active volume minimization and minimum PM usage are assumed as the goals to maximize the torque density and minimize the torque ripple and costs. Using dedicated codes, different rotor geometries are automatically generated and FEA is used to calculate the motor performance.

By utilizing the sequential quadratic programming (SQP) optimization method, the final design values are calculated and presented in Table IV. Considering the obtained design values in Tables III and IV, a final design for PMaSynRM is established. To validate the design accuracy and investigate the machine performance, an FEA-based study accompanied by the actual test results is presented in Section IV.

IV. FEA, FABRICATION, AND EXPERIMENTAL VALIDATION FOR THE FINALLY DESIGNED PMASYNRM

The final PMaSynRM design is further analyzed using an FEA-based commercial software package. The final design structure is shown in Fig. 7(a). The PMaSynRM design fulfills the mechanical requirements of the considered e-bike such as the outer and inner diameters. Due to the local saturation, the mesh should be finer in small parts such as ribs than in other regions. Fig. 7(b) shows that the mesh and magnetic flux density distribution form a magnetostatic simulation with 16-A phase current for one pole of the PMaSynRM. Paying attention to the magnetic limitation of the implemented laminated steels (1.7 T in simulation), the flux density distribution is convincing. By checking and validating the magnetic design accuracy through state operation, the important output parameters, such as the back EMF and average torque, are extracted from the postprocessing steps and are presented in the following discussions FEA, and one pole of the designed machine is analyzed in steady state.

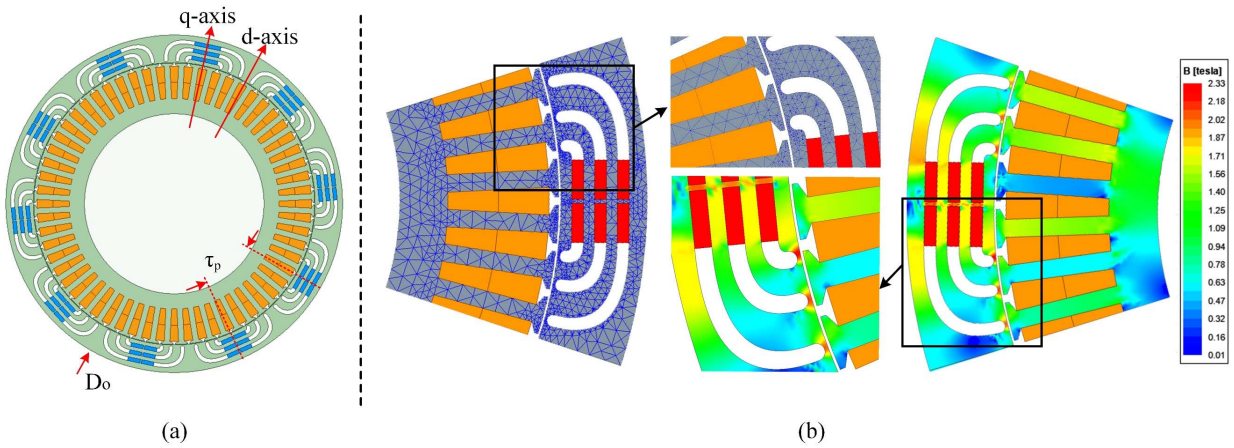

Fig. 7. Final design of PMaSynRM. (a) Top view of the designed PMaSynRM with *dq*-axes directions and pole pitch. (b) Mesh grid and flux density distribution of one pole for the designed structure.

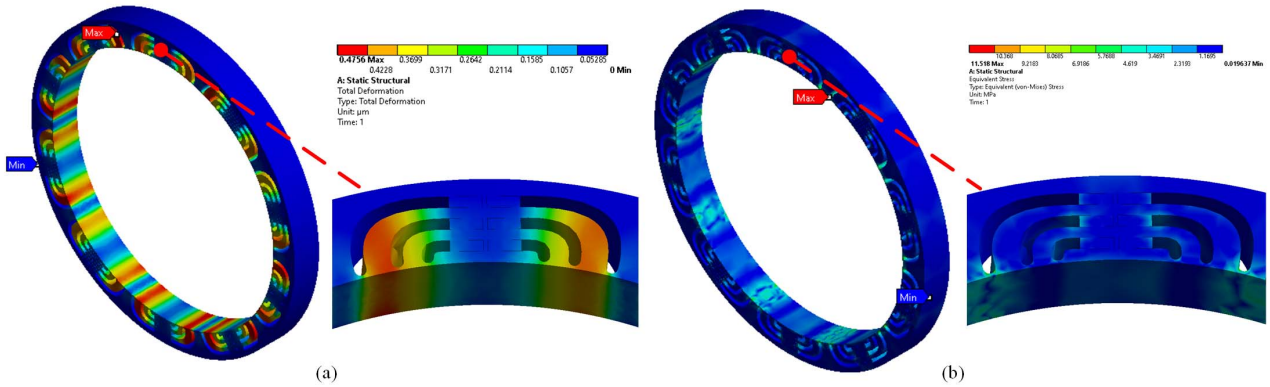

Fig. 8. Mechanical analysis of rotor at maximum speed (1800 r/min). (a) Total deformation. (b) Equivalent (von Mises) stresses.

After finalizing the shape and configuration of the rotor lamination in an electromagnetic analysis process, a mechanical analysis under centrifugal forces has been carried out where the total deformation and equivalent stress (von Mises) analyses are extracted. These results for the final rotor geometry in maximum rotor speed of 1800 r/min are presented in Fig. 8(a) and (b). The maximum total deformation is 0.48 μm and the equivalent (von Mises) stress is 11.52 MPa, which occurs in the tangential rib.

To validate the machine performance, the extracted parameters are compared with the experimental results for the prototyped machine. The various parts of the fabricated motor are presented in Fig. 9. The stator and rotor laminations are made of M470 silicon steel. The stator laminations are produced by the laser-cut process and assembled in the final skewed shape with a skewing mold fixture. The stator skew angle is six mechanical degrees. The rotor has ten poles where each pole has three flux barriers filled by the N35 PMs. An aluminum holder assembles the stator on a steel shaft. It should be noted that, to make the wiring process easier, seven parallel AWG 22 wires are used instead of one AWG 14 conductor. Each of the final stator phases consists of 20 coils and the resistance per phase of 0.48 Ω. The finalized stator is fixed on the in-wheel stator holder with a closed mechanical tolerance to avoid any vibration.

The rotor laminations are produced by the wire-cut process to keep the sizing accuracy of the flux barriers. After assembling the rotor final laminations, the PMs are inserted into the flux barriers with a strong adhesive material.

The finalized stator and rotor are assembled inside the designed caps by means of the stationary shaft. The finally prototyped PMaSynRM is connected to a real wheel installed on the provided test setup, as shown in Fig. 10. As seen, the assembled wheel is connected to a load via a rear derailleur and chain to replicate the real driving conditions.

A 500-W three-phase BLDCM is used as a load in the generator mode. By connecting the output terminals of the generator to the resistive loads, the various operating conditions for testing and performance validation of the PMaSynRM are provided.

In order to extract the output characteristics of the prototyped PMaSynRM, an accurate transducer is connected to the transmission system and load via a pair of spring coupling to preserve the sensitive torque meter shafts from mechanical unbalances. The PMaSynRM is driven and controlled by a TI DRV8301-69 M evaluation board. Using this board, the

Fig. 9. Different parts of the prototyped PMaSynRM.

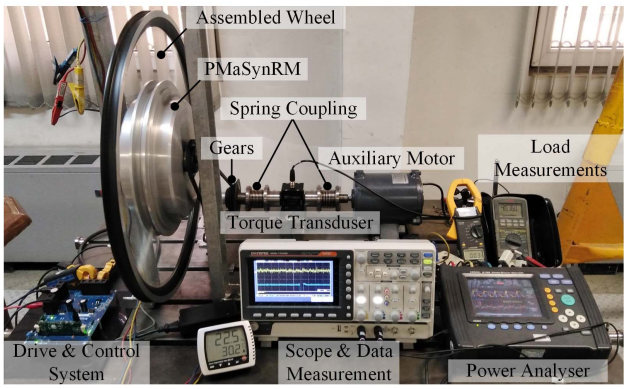

Fig. 10. Experiment setup for the PMaSynRM performance validation.

prototyped PMaSynRM is tested in a wide range of speeds and torques with a sensorless driving method. A power analyzer is utilized to observe and measure the motor voltage, current, and input power. All measured signals are saved and plotted by a digital four-channel oscilloscope and data acquisition system. An extra voltmeter and amperemeter are used to measure the load parameters. It is worth noting that the same test setup is used for the Golden Motor MP2 BLDCM experimentation in Section V.

Fig. 11(a) shows the simulated and experimental back EMF line-to-line voltages of the designed PMaSynRM at 200 r/min. The prototyped motor has been designed to achieve a 24-V voltage at a base speed of 200 r/min. As seen, the extracted line-to-line terminal voltage waveform is acceptably close to the FEA results and the maximum difference between FEA and measurements values is less than 1 V. From the tests, the

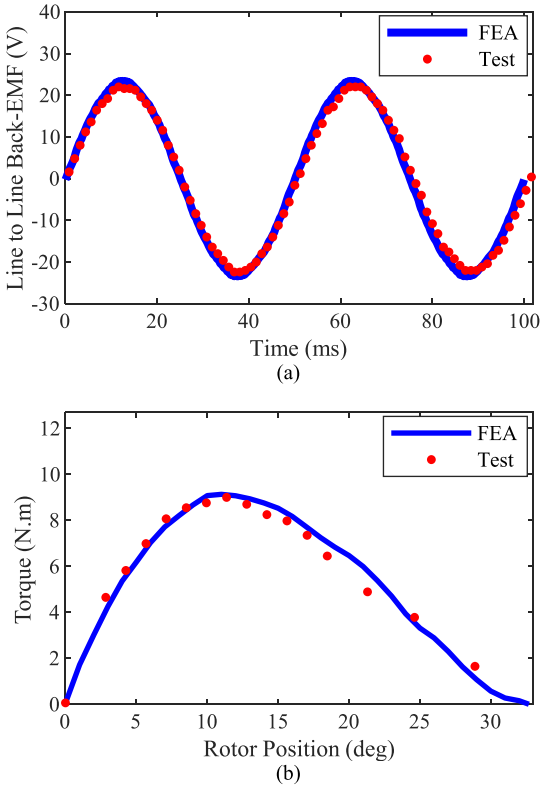

Fig. 11. Test versus FEA simulation. (a) Line-to-line back EMF. (b) Static torque.

peak value of PM flux linkage is computed as $\lambda_{\rm PM} = 0.35$ Wb and the simulation one is 0.37 Wb, so there is less than 5.5% discrepancy between the predictions and test results on PM flux linkage, which is mainly due to the lower magnet flux density in test condition and real materials. The standard static torque evaluation can validate the electrical design. The static torques in different rotor positions are presented in Fig. 11(b). To measure the static torques, phase A is connected to the positive polarity and phases B and C are connected in parallel to the negative polarity of a 10.8-V adjustable dc voltage source. As seen, the maximum torque is obtained near eight mechanical degrees (40 electrical degrees).

As the motor runs to produce maximum torque in each loading condition, additional measurements are captured close to the maximum torque point. The matching between measurement and predictions is satisfactory and errors can be related to the mechanical transmission system, i.e., gears and chains.

The average torque variation versus loading is shown in Fig. 12. This figure confirms the PMaSynRM expected capability in terms of electromagnetic torque, with maximum observed error between the predicted torques and actual torques in various loading conditions being less than 3%–4%.

V. Experimental Performance Comparison Between the Commercial BLDCM and Designed PMaSynRM

To have a better illustration on the advantages and shortcomings of the proposed PMaSynRM for e-bike propulsion, an experimental comparison between the commercial BLDCM and the prototyped PMaSynRM is provided in this section.

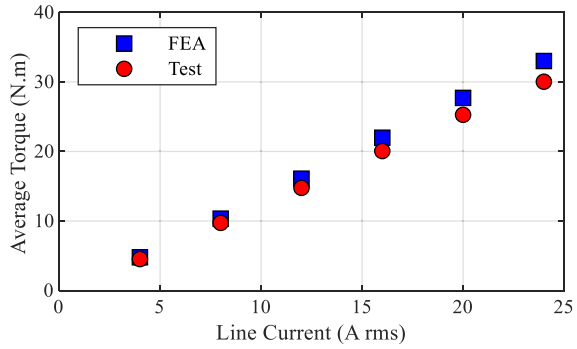

Fig. 12. Average torques versus line currents.

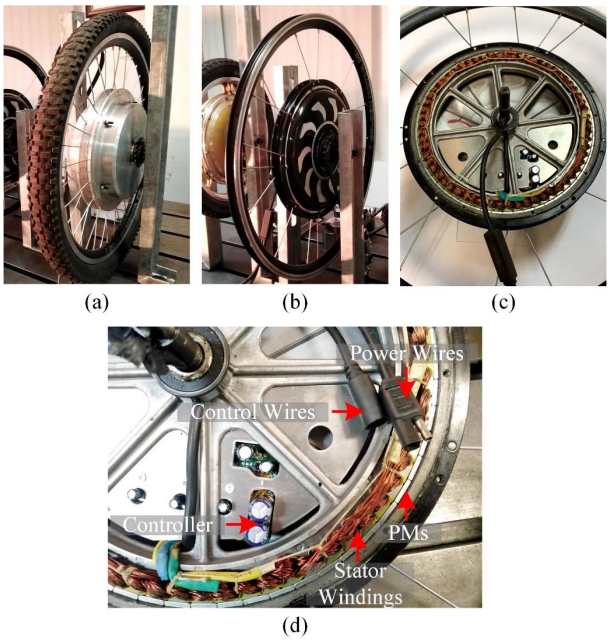

Fig. 13. Tested commercial BLDCM and PMaSynRM. (a) Prototyped PMaSynRM in wheel. (b) BLDCM in wheel. (c) BLDCM with the font cap opened. (d) BLDCM's components.

TABLE V
SUMMARY OF THE COMPARISON BETWEEN BLDCM AND PMASYNRM

Parameter	Unit	PMaSynRM	BLDCM
Overall volume	L	3.13	4.02
Power density	W/L	159.74	124.38
PM volume	mm^3	45000	63000
PM cost [a]	$	25.65	35.91

a.[23]

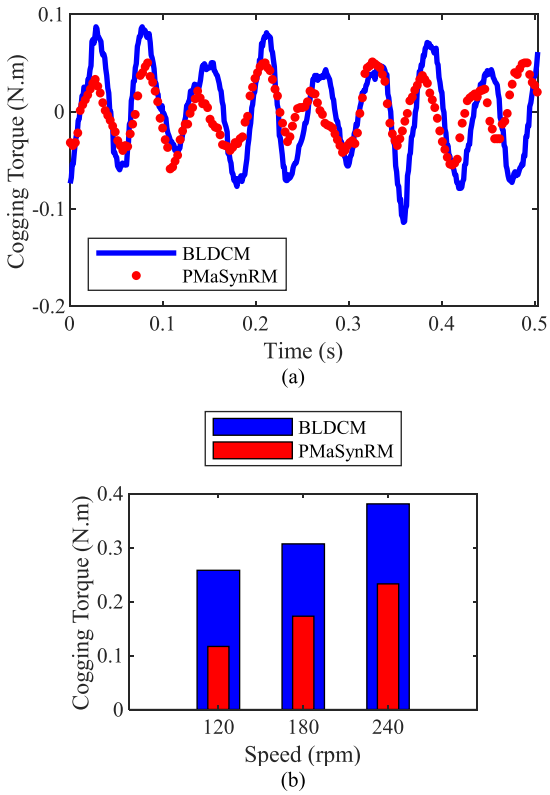

Fig. 14. Measured cogging torques for the deisgned PMaSynRM and commercial BLDCM. (a) Instantaneous cogging torques at 60 r/min. (b) Peak–peak cogging torques at different speeds.

To this end, the commercial 500-W, 200-r/min MP2 BLDCM is selected from Golden Motor's products with an internal drive system.

Both motors are assembled on a wheel and are presented in Fig. 13(a) and (b). The internal view of BLDCM with the front cap opened, and the winding configuration and PM arrangement are presented in Fig. 13(c) and (d), respectively. The summary of the comparisons in terms of volume, power density, and PM total cost is given in Table V. As shown in Table V, 40% higher amount of magnets is used in BLDCM compared to the designed PMaSynRM, which makes it more expensive than the PMaSynRM [24]. Due to the significant difference between the PMs used in the investigated machines, the PM total cost for the BLDCM is 40% higher than that for PMaSynRM counterpart. In addition, the total active volume of the designed PMaSynRM is 23% smaller than the commercial BLDCM, which causes the torque density of the designed and tested PMaSynRM to be about 28% larger than the BLDCM.

The higher cogging torque causes a higher output torque ripple, which can result in noise, especially at low speeds at which the inertia cannot adequately smooth the output torque profile like for e-bikes [25]. As the riders are very close to the electric motor without any measure to reduce the acoustic noise, cogging torque evaluation and reduction are important in e-bike applications.

The measured cogging torques for the designed PMaSynRM and BLDCM at 60 r/min (28% of nominal speed) are shown in Fig. 14(a). The peak–peak cogging torque values are 0.1 and 0.2 N · m for PMaSynRM and BLDCM, respectively. The peak–peak cogging torque values at some example higher speeds are shown in Fig. 14(b). As seen, the PMaSynRM has lower cogging torques at all speeds. The main reason for having a lower cogging torque in the designed and tested PMaSynRM compared to the commercial BLDCM is because of the less volume of PMs used in the final design of the PMaSynRM and the constraints provided during the design steps to keep the PMs usage minimized and to provide at least half of the total torque of the PMaSynRM through the reluctance torque component.

The measured instantaneous torque and speed responses for both designed PMaSynRM and commercial BLDCM at

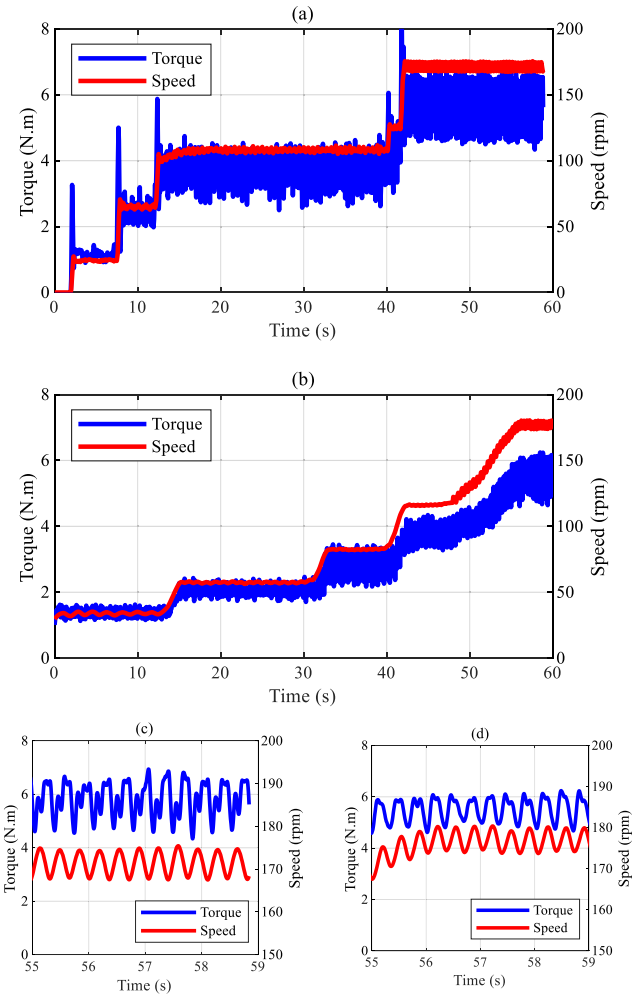

Fig. 15. Instantaneous torque and speed responses for the tested PMaSynRM and commercial BLDCM. (a) BLDCM. (b) PMaSynRM. (c) Zoomed in responses for BLDCM. (d) Zoomed in responses for PMaSynRM.

various operating speeds and loading conditions are shown in Fig. 15. The curves are magnified in Fig. 15(c) and (d) for the tested BLDCM and PMaSynRM, respectively. These two subfigures highlight the torque and speed oscillations. As seen at almost the same average torque and speed, the torque and speed oscillations for the designed PMaSynRM are lower than for the BLDCM. The speed oscillations are 1.4% and 2% and the torque oscillations are 14% and 22% for the designed PMaSynRM and commercial BLDCM, respectively. In other words, the startup process with the designed PMaSynRM will be smoother than with the BLDCM.

Although the efficiency maximization has not been considered as one of the goals during the machine design steps in this article, additional comparisons on the efficiencies of tested PMaSynRM and BLDCM at various speeds and loadings are highlighted in Table VI. In this table, N_m, P, and $I_{\rm dc}$ represent the mechanical speed, output power, and battery current, respectively. As seen for almost the same output powers and at the same speeds, the BLDCM shows a 5.9%–12.2% better efficiency than the PMaSynRM. The power factor for higher output powers is larger than in lower loading conditions.

TABLE VI

EXPERIMENTAL EFFICIENCY COMPARISON IN VARIOUS OPERATING POINTS

Motor	N_m (rpm)	T (N.m)	I_{dc} (A)	P (W)	*Eff.* (%) [a]
PMaSynRM	160	5.62	4.27	94.16	67.74
	207	7.04	6.68	152.60	67.81
	190	9.78	8.78	194.59	65.03
	210	20.50	20.35	450.82	63.30
BLDCM	160	5.70	3.07	95.50	80.01
	207	7.11	4.97	154.12	79.80
	190	9.58	6.65	190.61	73.80
	210	20.12	16.46	442.46	69.20

a. Motor with transmission system

The comparisons provided show the superiority of the PMaSynRM over the BLDCM for e-bike propulsion in terms of lower PM usage and corresponding cost reduction and environmental effects, smaller torque ripple and speed oscillations, and larger power density. The toll to be paid for such advantages is a relatively lower efficiency, especially at low loading conditions.

VI. CONCLUSION

Not so far covered in the existing public literature and industry reports, an outer rotor PMaSynRM has been designed and tested to replace a commercial BLDCM for e-bike applications. The main goal in the design stage was to have a lower volume of PMs in the PMaSynRM structure to reduce the cost, torque ripple, and environmental issues typical of PM machines. The PM reduction has been possible by providing around one half of the total torque in the PMaSynRM through the reluctance torque component. The overall torque density of the PMaSynRM has been increased by reducing the total active volume of the machine compared to the existing dimensions of the BLDCM. The mechanical analysis shows that the maximum total deformation is lower than 0.048% of the air-gap length and the maximum equivalent (von Mises) stress is 11.52 MPa at the maximum possible speed of 1800 r/min, which is far below the yield strength of M470 Silicon steel lamination used in the rotor structure, which is between 300 and 350 MPa. Through simulations and experimental performance assessment of the two machines, it was illustrated that the designed PMaSynRM can increase the torque density by 28%, reduce the cogging torque and torque ripple by 50% and 8%, respectively, and reduce the PMs usage and corresponding cost by 40% compared to the commercial BLDCM. The drawback is a relatively lower efficiency due to the significantly lower volume of PMs utilized.

REFERENCES

[1] B. Bilgin *et al.*, "Making the case for switched reluctance motors for propulsion applications," *IEEE Trans. Veh. Technol.*, vol. 69, no. 7, pp. 7172–7186, Jul. 2020.

[2] Y. Xiao *et al.*, "A novel asymmetric interior permanent magnet machine for electric vehicles," *IEEE Trans. Energy Convers.*, vol. 36, no. 3, pp. 2404–2415, Sep. 2021.

[3] R. Nasiri-Zarandi and M. Ebrahimi, "Extracting requirements for design a two-wheels electric vehicle and proposing a design procedure," in *Proc. 9th Annu. Power Electron., Drives Syst. Technol. Conf. (PEDSTC)*, Feb. 2018, pp. 462–468.

[4] G. Rose and P. Cock, *Encouraging E-Bike Use: The Need for Regulatory Reform in Australia*. Clayton, VC, USA: Institute of Transport Studies, Monash Univ., 2003.
[5] *Approval and Market Surveillance of Two-or Three-Wheel Vehicles and Quadricycles*, document EU 168/2013, 2013.
[6] *Requirements for Low-Speed Electric Bicycles*, document Public Law 107-319, Dec. 2002.
[7] J. Lin, N. Schofield, and A. Emadi, "External-rotor 6–10 switched reluctance motor for an electric bicycle," *IEEE Trans. Transport. Electrific.*, vol. 1, no. 4, pp. 348–356, Dec. 2015.
[8] Y. Yang, M. M. Rahman, T. Lambert, B. Bilgin, and A. Emadi, "Development of an external rotor V-shape permanent magnet machine for E-bike application," *IEEE Trans. Energy Convers.*, vol. 33, no. 4, pp. 1650–1658, Dec. 2018.
[9] N. Bianchi, S. Bolognani, E. Carraro, M. Castiello, and E. Fornasiero, "Electric vehicle traction based on synchronous reluctance motors," *IEEE Trans. Ind. Appl.*, vol. 52, no. 6, pp. 4762–4769, Nov./Dec. 2016.
[10] K. Wang, Z. Q. Zhu, and G. Ombach, "Torque enhancement of surface-mounted permanent magnet machine using third-order harmonic," *IEEE Trans. Magn.*, vol. 50, no. 3, pp. 104–113, Mar. 2014.
[11] R. Krishnan, *Permanent Magnet Synchronous and Brushless DC Motor Drives*. Boca Raton, FL, USA: CRC Press, 2017.
[12] J. Faiz, M. Heidari, and H. Sharafi, "Torque ripple and switching frequency reduction of interior permanent magnet brushless direct current motors using a novel control technique," *IET Power Electron.*, vol. 12, no. 14, pp. 3852–3858, Nov. 2019.
[13] *Cycles Electrically Power Assisted Cycles EPAC Bicycles*, document EN 15194, Oct. 2017.
[14] T. Wang, X. Zhu, S. Zheng, L. Quan, Z. Xiang, and X. Zhou, "Investigation on torque characteristic and PM operation point of flux-intensifying PM motor considering low-speed operation," *IEEE Trans. Magn.*, vol. 57, no. 2, pp. 1–5, Feb. 2021.
[15] S. P. Nikam, V. Rallabandi, and B. G. Fernandes, "A high-torque-density permanent-magnet free motor for in-wheel electric vehicle application," *IEEE Trans. Ind. Appl.*, vol. 48, no. 6, pp. 2287–2295, Nov. 2012.
[16] K. M. Rahman, B. Fahimi, G. Suresh, A. V. Rajarathnam, and M. Ehsani, "Advantages of switched reluctance motor applications to EV and HEV: Design and control issues," *IEEE Trans. Ind. Appl.*, vol. 36, no. 1, pp. 111–121, Jan./Feb. 2000.
[17] B. Howey, B. Bilgin, and A. Emadi, "Design of an external-rotor direct drive E-bike switched reluctance motor," *IEEE Trans. Veh. Technol.*, vol. 69, no. 3, pp. 2552–2562, Mar. 2020.
[18] G. Pellegrino, T. M. Jahns, N. Bianchi, W. Soong, and F. Cupertino, *The Rediscovery of Synchronous Reluctance and Ferrite Permanent Magnet Motors Tutorial Course Notes*, vol. 1. Cham, Switzerland: Springer, 2016.
[19] S. Morimoto, M. Sanada, and Y. Takeda, "Performance of PM-assisted synchronous reluctance motor for high-efficiency and wide constant-power operation," *IEEE Trans. Ind. Appl.*, vol. 37, no. 5, pp. 1234–1240, Sep. 2001.
[20] G. Bacco, N. Bianchi, and H. Mahmoud, "A nonlinear analytical model for the rapid prediction of the torque of synchronous reluctance machines," *IEEE Trans. Energy Convers.*, vol. 33, no. 3, pp. 1539–1546, Sep. 2018.
[21] C.-S. Jin, D.-S. Jung, K.-C. Kim, Y.-D. Chun, H.-W. Lee, and J. Lee, "A study on improvement magnetic torque characteristics of IPMSM for direct drive washing machine," *IEEE Trans. Magn.*, vol. 45, no. 6, pp. 2811–2814, Jun. 2009.
[22] A. Nobahari, A. Vahedi, and R. Nasiri-Zarandi, "A modified permanent magnet-assisted synchronous reluctance motor design for torque characteristics improvement," *IEEE Trans. Energy Convers.*, vol. 37, no. 2, pp. 989–998, Jun. 2022, doi: 10.1109/TEC.2021.3127081.
[23] S. S. Maroufian and P. Pillay, "Design and analysis of a novel PM-assisted synchronous reluctance machine topology with AlNiCo magnets," *IEEE Trans. Ind. Appl.*, vol. 55, no. 5, pp. 4733–4742, Sep. 2019.
[24] Y. Wang, G. Bacco, and N. Bianchi, "Geometry analysis and optimization of PM-assisted reluctance motors," *IEEE Trans. Ind. Appl.*, vol. 53, no. 5, pp. 4338–4347, Sep. 2017.
[25] S. Leitner, H. Gruebler, and A. Muetze, "Cogging torque minimization and performance of the sub-fractional HP BLDC claw-pole motor," *IEEE Trans. Ind. Appl.*, vol. 55, no. 5, pp. 4653–4664, Sep. 2019.

Reza Nasiri-Zarandi (Member, IEEE) was born in Khodabandeh, Iran, in 1985. He received the B.S. degree from the K. N. Toosi University of Technology, Tehran, Iran, in 2008, the M.S. degree in electrical engineering from Tafresh University, Tafresh, Iran, in 2010, the Ph.D. degree in electrical engineering from the Amirkabir University of Technology, Tehran, and the double Ph.D. degree from Politecnico di Torino, Turin, Italy, in 2015.

From 2015 to 2016, he was a Post-Doctoral Researcher with the Electrical Machines and Transformers Research Laboratory (EMTRL), Electrical Engineering Department, Amirkabir University of Technology (Tehran Polytechnic), Tehran. He is currently a Faculty Member and the Head of the Electrical Machine Research Department and the Electrical Machine Research Laboratory, Niroo Research Institute, Tehran. His research interests include design, modeling, finite-element analysis (FEA), optimization, prototyping, control and drive of rotating electric machines, and power electronics.

Ahmadreza Karami-Shahnani (Member, IEEE) was born in Darab, Iran, in 1998. He received the B.Sc. degree in electrical engineering from the K. N. Toosi University of Technology, Tehran, Iran, in 2020, where he is currently pursuing the M.Sc. degree in power electronics and electrical machine design.

Since 2020, he has been a part-time Researcher with the Electrical Machines Research Department, Niroo Research Institute (NRI), Tehran. His research interests include the design, control, and analysis of electric machines, and power electronics for transportation electrification.

Mohammad Sedigh Toulabi (Senior Member, IEEE) was born in Khorramabad, Iran, in 1985. He received the B.Sc. degree from the K. N. Toosi University of Technology, Tehran, Iran, in 2007, the M.Sc. degree from Shahid Beheshti University, Tehran, in 2009, and the Ph.D. degree from the University of Alberta, Edmonton, AB, Canada, in 2016, all in electrical engineering.

From May 2015 to December 2015, he was a Visiting Graduate Student at the Department of Electrical and Computer Engineering, University of Calgary, Calgary, AB, Canada. From July 2016 to February 2019, he was a Senior Research Associate with the University of Manitoba, Winnipeg, MB, Canada. From February 2019 to September 2020, he was an Electrified Powertrain Lead Engineer with Fiat Chrysler Automobiles (FCA), US LLC, Auburn Hills, MI, USA. He is currently an Assistant Professor and the Deputy Director of the Center for Hybrid Automotive Research and Green Energy (CHARGE) Laboratory, Department of Electrical and Computer Engineering, University of Windsor, Windsor, ON, Canada. His research interests include the design, analysis, modeling, control, and testing of electric machines, and power electronics for transportation electrification.

Dr. Toulabi is an Associate Editor of the IEEE TRANSACTIONS ON ENERGY CONVERSION, IEEE TRANSACTIONS ON TRANSPORTATION ELECTRIFICATION, and IEEE POWER ENGINEERING LETTERS and a registered Professional Engineer (P.Eng.) in Ontario, Canada.

Alberto Tessarolo (Senior Member, IEEE) received the Laurea degree in electrical engineering from the University of Padova, Padua, Italy, in 2000, and the Ph.D. degree in electrical engineering from the University of Trieste, Trieste, Italy, in 2011.

He worked in the industry in the design and development of large innovative motors, generators, and drives. Since 2006, he has been with the Engineering and Architecture Department, University of Trieste, where he currently teaches the courses in electric machine fundamentals and electric machine design as a Full Professor. He has authored over 180 international articles in the areas of electrical machines and drives.

Dr. Tessarolo served as an Associate Editor for the IEEE TRANSACTIONS ON INDUSTRY APPLICATIONS and *IET Electric Power Applications* from 2016 to 2021. He is currently the Editor-in-Chief of the IEEE TRANSACTIONS ON ENERGY CONVERSION.